Check for updates

Synthesis of Wet-Chemically Prepared Porous-Graphene Single Layers on Si/SiO₂ Substrate Increasing the Photoluminescence of MoS₂ in Heterostructures

*Yiqing Wang, Christof Neumann, Marleen Hußmann, Qing Cao, Yalei Hu, Oisín Garrity, Patryk Kusch, Andrey Turchanin, and Siegfried Eigler**

Wet-chemical generation of pores in graphene is a challenging synthetic task. Although graphene oxide is available in large quantities and chemically diverse, extended lattice defects already present from synthesis hamper the controlled growth of pores. However, membrane, energy, or nanoelectronic applications essentially require uniform pores in applications. Here, oxo-functionalized graphene (oxoG), a type of graphene oxide with a controlled density of vacancy defects, is used as starting material. Pores in graphene are generated from potassium permanganate treated oxoG and heating from room temperature to 400 °C. With etching time, the size of pores increases and pore-diameters of, for example, 100–200 nm in majority become accessible. The experiments are conducted on the single-layer level on Si/SiO₂ wafers. Flakes remain stable on the μm scale and do not fold. The process leads to rims of pores, which are functionalized by carbonyl groups in addition to hydroxyl and carboxyl groups. In addition, it is found that heterostructures with intrinsically n-doped MoS₂ can be fabricated and photoluminescence (PL) measurements reveal a 10-fold increased PL. Thus, graphene with pores is a novel highly temperature-stable electron-accepting 2D material to be integrated into van der Waals heterostructures.

Y. Wang, M. Hußmann, Q. Cao, Y. Hu, Prof. S. Eigler
Institute of Chemistry and Biochemistry
Freie Universität Berlin
Takustraße 3, 14195 Berlin, Germany
E-mail: siegfried.eigler@fu-berlin.de
Dr. C. Neumann, Prof. A. Turchanin
Institute of Physical Chemistry
Center for Energy and Environmental Chemistry (CEEC) Jena
Friedrich Schiller University Jena
Lessingstraße 10, 07743 Jena, Germany
O. Garrity, Dr. P. Kusch
Department of Physics
Freie Universität Berlin
Arnimallee 14, 14195 Berlin, Germany

1. Introduction

Graphene with defects, such as pores in the lattice of graphene[1–3] finds emerging applications for water separation, gas separation and purification, or sensing.[4–10] The chemical functionalization of graphene can either be accomplished with graphene dispersed in solvents,[11] or with graphene deposited on surfaces.[12] Applications based on bulk functionalization target, for example, composite formation, exploiting the mechanical properties of graphene, or electronic properties for energy applications and energy conversion or storage.[13–19] In particular sensing applications are targeted using graphene, which is deposited on surfaces. Thereby, functionalization of deposited graphene can in principle occur on the surface or at the rim of flakes. However, since investigated sensing devices typically have μm dimensions, functionalization at rims of flakes is supposed to have only little influence on the device performance. With drilling pores into the graphene lattice, the proportion of rims can be increased. In principle, pores can be etched using focused ion beam and the approach allows for regular patterning, shape, and size control.[16,20–22] Thereby, the successful patterning is a technological challenge. Since the focused ion beam also interacts with the substrate the dielectric layer, such as SiO₂ may become damaged. Thus, although that approach is appealing, it bears some drawbacks, since high-end technology is required.[16,23]

The growth of pores in graphene on the single-layer level is described by numerous methods in the literature in particular etching methods.[24] Nanometer-sized pores were created in graphene by oxygen plasma or other plasmas.[25,26] Moreover, pores on the nanoscale were created in few-layered graphene using oxygen, ozone, or liquid phase etching using HNO₃ solution as etching reagents.[26–28] In addition, it is reported that a single Ni atom can be used to cut graphene to a nanomesh with a pore size of about 10–50 nm.[29] Sub-nanometer diameter pores in single-layer graphene membranes were also fabricated, accordingly, defects were introduced into the graphene lattice through ion bombardment and oxidative etching enlarged defects into pores with sizes of 0.40 ± 0.24 nm.[30,31] Moreover, also graphene oxide

**ADVANCED
SCIENCE NEWS**
www.advancedsciencenews.com

**ADVANCED
MATERIALS
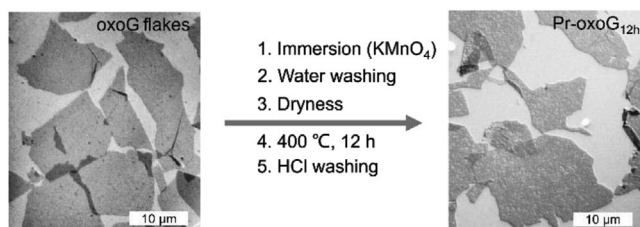INTERFACES**
www.advmatinterfaces.de

Figure 1. Scheme describing the fabrication of pores starting from oxoG. Flakes of oxoG are deposited on a Si/SiO$_2$ substrate. Pr-oxoG$_{12h}$ is fabricated from oxoG, immersed in KMnO$_4$ solution, followed by washing, drying, and annealing in argon atmosphere at 400 °C for 12 h. The white scale bar relates to 10 μm in optical microscopy images.

was used as precursor for etching pores, however, no uniform size was reported and the size of pores is limited to few nm, assumedly due to too many lattice defect sites already present in common graphene oxide, which act as origins for etching. Thus, the formation of larger pores is not possible, since flakes start to disintegrate.[28,32–35] Accordingly, graphene oxide with extended lattice defects conceptionally can't be considered as a precursor for generating graphene with pores of reasonable lateral dimensions, of tens to hundreds of nm (Table S1, Supporting Information). Here we describe the formation of pores of circular shape by a Mn-species assisted etching procedure at 400 °C in argon atmosphere. The approach starts from oxo-functionalized graphene (oxoG) with a low density of initial vacancy defects (0.8%, as determined by Raman spectroscopy), which is a subclass of the graphene oxide family. By controlling the reaction conditions, it is possible to gain a certain control over the formation of pores with diameters between 100–200 nm in majority. Those pore-graphene materials are highly temperature stable since they are synthesized at 400 °C. Moreover, integration into heterostructures is possible. We report that the amplitude of the photoluminescence (PL) signal of MoS$_2$ enhances 10-times.

2. Results and Discussion

The formation of pores in monolayers of oxoG was elaborated in a five-step procedure (**Figure 1**). Accordingly, oxoG flakes are deposited on Si/300 nm SiO$_2$ wafer by Langmuir–Blodgett technique.[36–38] The lateral dimensions of monolayer oxoG flakes are roughly 20 μm (Figure 1 left and Figure S2A–C, Supporting Information). Figure S1A,B, Supporting Information, show the results of the statistical Raman analysis of flakes of reduced oxoG revealing an I_D/I_G ratio of the defect induced D band and the G band of 2.7 ± 0.14 and a full-width at half-maximum (Γ) of the 2D band $\Gamma_{2D} = 93 \pm 9$ cm^{-1}. Thus, the average distance of defects L_D is about 2 nm, following the relation introduced by Lucchese and Cançado.[39,40] The distance of defects can be related to a density of defects of about 0.8%.

Then the wafer was immersed into a solution of potassium permanganate (KMnO$_4$) overnight (for details see experimental part). Metal ions are bound to the surface of the single-layers of oxoG on Si/SiO$_2$ substrates. A study based on the roughness analysis performed by atomic force microscopy (AFM) was conducted focusing on one specific flake of oxoG before and after KMnO$_4$ immersion (step 1 in Figure 1) and finally after washing the surface with water (step 2 in Figure 1, see also Figure S2,

Supporting Information). Line height scans indicate that the root mean square roughness of the surface increases from about 0.14 nm to about 0.39 and 0.32 nm, respectively. As we showed before, organosulfate groups with hydronium counter ions explain the thickness of flakes of oxoG.[41] Here, we propose that hydronium ions are exchanged by Mn-species. Although we realized that step 2, washing the wafer with water to remove possible excess or loosely bound Mn-species is essential for the controlled growth of pores, the AFM height profile remains similar (Figure S2F, Supporting Information) with a roughness of 0.32 nm. After drying the sample at room temperature, the annealing process was carried out in a tube furnace in argon at 400 °C for 12 h. Afterward, the annealed material on the wafer was washed with 1 M hydrochloric acid (HCl) to remove metal or metal oxide particles.[33] The annealing process induces the disproportionation reaction of oxoG, and we identified in an earlier study that pores can grow by the release of CO$_2$, while intact graphene patches with diameters of around 3 nm in diameter are generated, as a consequence of mobile oxo-groups on the lattice of graphene.[42] However, by the here described procedure, graphene with pores (Pr-oxoG$_{12h}$; index indicated the annealing time) is generated with much larger pores.

By varying the annealing time, graphene materials with pores of different sizes are generated. The formed pores can be visualized by AFM and optical microscopy, respectively. Here, through comparative experiments, we can confirm that manganese plays a very important role in the formation process of pores. For single layers, we suggest that there are small nanoparticles at the edges of pores. Because of the little amount, the content is below the detection limit of, for example, X-ray photoelectron spectroscopy (XPS) or Raman (Mn−O vibrations, Figure S6A, Supporting Information). We further assume that the metal particles move along the edge of the pore to continuously catalyze the pore formation leading to increased diameters of pores. Accordingly, based on this assumption it can be explained why round pores are formed, and thus, the size of the pores can be controlled by etching-time. Figure S3A, Supporting Information, shows an AFM image of single-layer oxoG with no visible pores in the zoomed area depicted in Figure S3B, Supporting Information. As we visualized before by transmission electron microscopy at atomic resolution, oxoG bears only one or few atom vacancies.[42,43] Figure S3C,D, Supporting Information, show AFM images of Pr-oxoG$_{6h}$. The presence of small pores is visible in Figure S3D, Supporting Information. To make the comparison reliable, we analyzed the same flake and same area of the flake before and after annealing. Therefore, we conclude that there are small pores of 45 ± 24 nm formed in Pr-oxoG$_{6h}$, as can be observed from Figure S3D and Table S2, Supporting Information.[30]

Extending the annealing time from 6 to 12 h results in the formation of larger pores (Pr-oxoG$_{12h}$). Pores in Pr-oxoG$_{12h}$ on Si/SiO$_2$ substrates are visible under the optical microscope (**Figure 2**A). As shown in the AFM image of Figure 2B, (the stacked square is visible in the center with higher resolution) there are many pores distributed over the entire flake. An AFM image with a further enlarged area of the flake of Pr-oxoG$_{12h}$ is depicted in Figure 2C. The circular shape of pores with an apparently uniform size of 147 ± 73 nm is clearly visible (Table S2, Supporting Information). The height of Pr-oxoG$_{12h}$ is about 1.4 nm, as measured by the AFM tip hitting the underneath surface
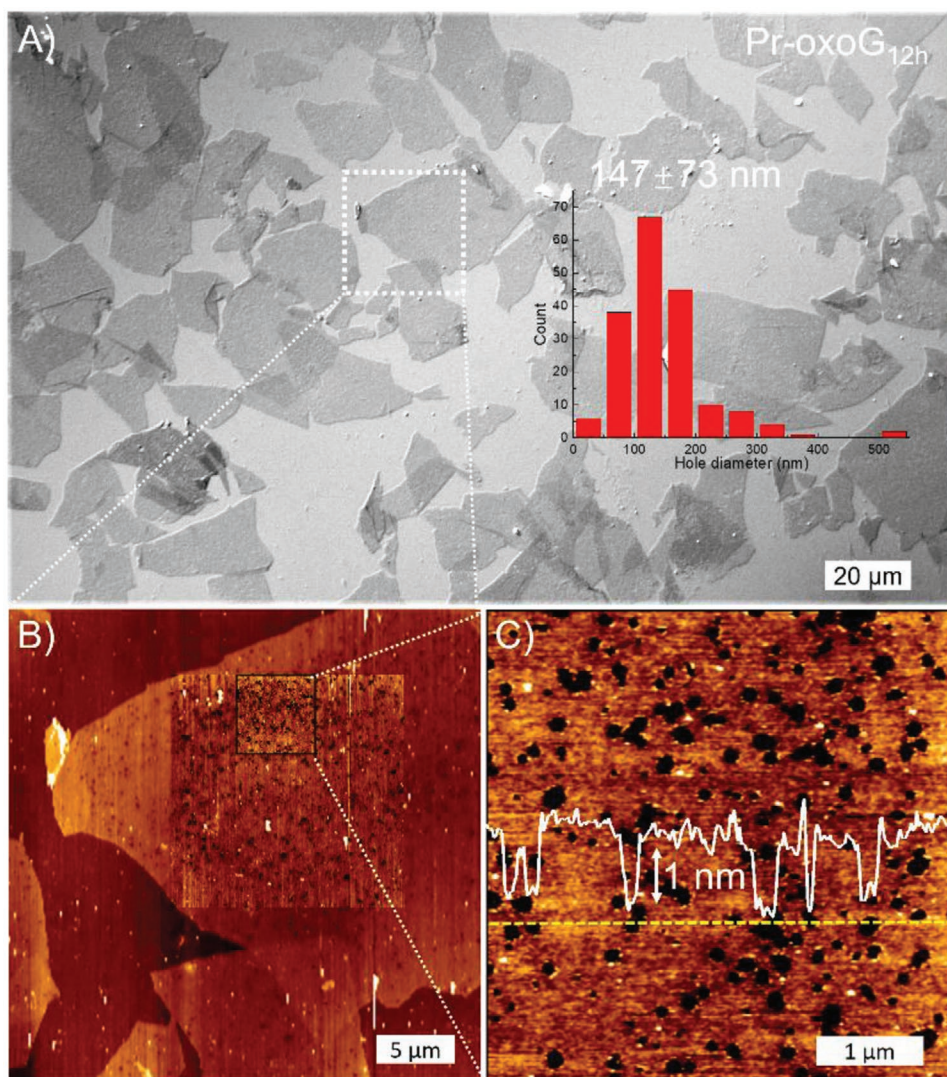
Figure 2. A) Optical microscopy image (differential interference contrast, DIC) of flakes of Pr-oxoG$_{12h}$ on Si/SiO$_2$ substrates. Inset: histogram shows the size distribution of pores shown in B and C, smaller than 50 nm are not counted. B) AFM topography image of Pr-oxoG$_{12h}$ with overlay of detailed scanned area; C) zoomed AFM topography image of (B) showing pores. White line: height profile, arrow indicates 1 nm.

through the pores. The results of the quantitative analysis of the lateral dimensions of pores in graphene are illustrated in the histogram shown in the inset of Figure 2A. The analysis reveals that the pores diameters are roughly 150 ± 70 nm.

Skipping the final step of HCl washing results in an increased height when measuring through a hole from the SiO$_2$ surface to the surface of graphene (**Figure 3**). We assume that a uniform hydration layer may be present between the substrate and graphene. We note that Mn-species, such as nanoparticles, supposed to be located at the rims of pores are not detected by AFM.[29,33] An analysis of the pore size before and after HCl washing indicates a little increase from 129 ± 75 to 147 ± 72 nm in Figure 3D. Those data are also listed in Table S2, Supporting Information. Next, a reference experiment was performed to eliminate the possibility that similar pores are formed using oxoG without the influence of Mn-species. Thus, flakes of oxoG were annealed for 12 h. As shown in Figure S4, Supporting Information, by optical microscopy and AFM, no

obvious large pores are observed. Therefore, we conclude that annealing alone is not leading to the formation of large pores, starting from oxoG.

To further investigate the effect of annealing time on the pore diameter, we further extended the processing time to 16 h. As shown in Figure S5, Supporting Information, large and merged pores are visible for Pr-oxoG$_{16h}$, both in the optical microscopy image of Figure S5A, Supporting Information, and AFM images of Figure S5B,C, Supporting Information. As shown in Figure S5B, Supporting Information, there are many pores in the flakes (enlargement in Figure S5C, Supporting Information) and the mean diameter is 168 ± 94 nm. To gain more insights into the mechanism of pore formation process was conducted on few-layers of oxo-G. The AFM images in Figure S6, Supporting Information, reveal some dots in the center of the pore. The thickness of the dots is basically the same as the material height. We suggest that those dots are either trapped etched carbon dots or manganese nanoparticles.
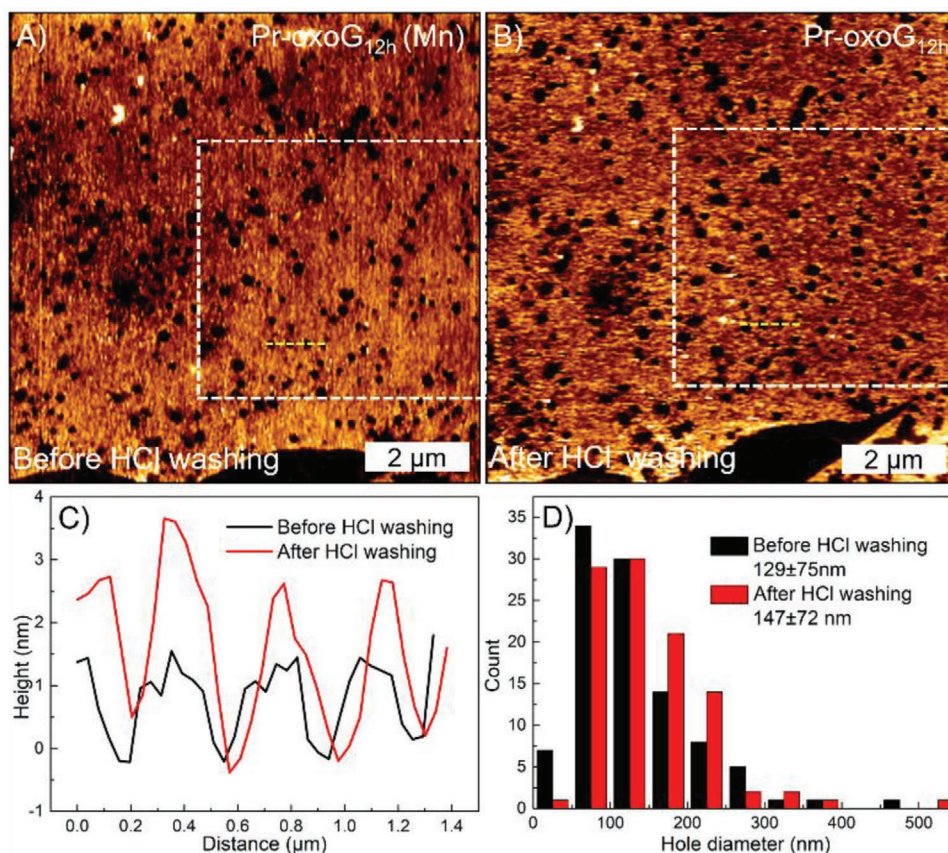
**ADVANCED
SCIENCE NEWS**
www.advancedsciencenews.com

**ADVANCED
MATERIALS
INTERFACES**
www.advmatinterfaces.de

Figure 3. AFM topography images in (A); before (Pr-oxoG$_{12h}$ (Mn)), and B) after (Pr-oxoG$_{12h}$) HCl washing. C) Height profiles of AFM images along yellow dashed lines. The black and red lines represent the pores height profiles of Pr-oxoG$_{12h}$ (Mn) and Pr-oxoG$_{12h}$, respectively. D) Distribution of pores in the white box. The black and red bars represent the pores quantity profiles of Pr-oxoG$_{12h}$ (Mn) and Pr-oxoG$_{12h}$.

Although, evidence is found supporting the hypothesis of the catalytical role of Mn-species such as Mn-atoms or nanoparticles, the final proof is a matter of further research.

A comparison between the different mean diameters and mean pore areas after different annealing time are shown in Figure S7, Supporting Information (data listed in the Table S2, Supporting Information). As the pyrolysis time increases, the average diameter and area of the pores increase according. In the process of growing pores, as shown in Figure 1, we pointed out that skipping washing step 2 with water results in a highly uncontrolled etching process. Compared with Figure 2A, the same annealing time of 12 h was chosen and the AFM image in Figure S8, Supporting Information, shows small pores, very large and also merged pores distributed all over the flakes. We suggest that Mn-species are unevenly distributed on the surface of oxoG if the water washing step is skipped. We note that we observed also partly destroyed and crumpled/folded layers. Therefore, we conclude that washing step 2 is essential to control the generation of pores, and to get some control over the uniformity of grown pores.

Next, an XPS study was conducted to analyze changes in the chemical composition of oxoG and Pr-oxoG$_{12h}$ (**Figure 4**). All XPS data are listed in Table S3. The high-resolution C 1s spectrum of oxoG in Figure 4A displays a typical saddle-like pattern, which stems from significant oxidation in oxoG.

The content of sp^2-C is about 47.8% (due to oxo-groups) and the content of C−O/C−OH/C=O is up to 46.3%. It can be seen from the high-resolution Mn 2p that there is no obvious peak in Figure 4E. Thus, few-layer oxoG contains less than 0.1 at% Mn. Before HCl washing, the high-resolution Mn 2p of Pr-oxoG$_{12h}$ (Mn) reveals also less than 0.1 at% Mn, as shown in Figure 4F. This finding further support that little quantities of Mn-species are catalytically active in the etching process. After annealing, the oxygen content of Pr-oxoG$_{12h}$ is significantly reduced compared to oxoG. As expected, the content of sp^2-C increased, here to 50.8%. The high-resolution O 1s spectrum of Pr-oxoG$_{12h}$ displays the peaks of C−O, C=O, O−C=O (Figure 4D). We note that the O 1s peak in Figure 4B is only for reference, since Pr-oxoG$_{12h}$ is not completely covering the Si/SiO$_2$ substrate and since large pores exist in Pr-oxoG$_{12h}$. Thus, the influence of the surface O-signal from SiO$_2$ is affecting the quantitative analysis. The oxygen content is significantly reduced in comparison to oxoG and close to zero if we consider its influence on SiO$_2$.[2,44,45] We note, for analyzing the C−O species the C 1s analysis is representative. The analyses of C 1s peaks reveal the formation of C=O and C−O/C−OH groups as a consequence of annealing and the accompanied growth of pores (Figure 4B). Thus, we conclude that the rims of pores are functionalized by carbonyl groups in addition to hydroxyl and carboxyl groups.
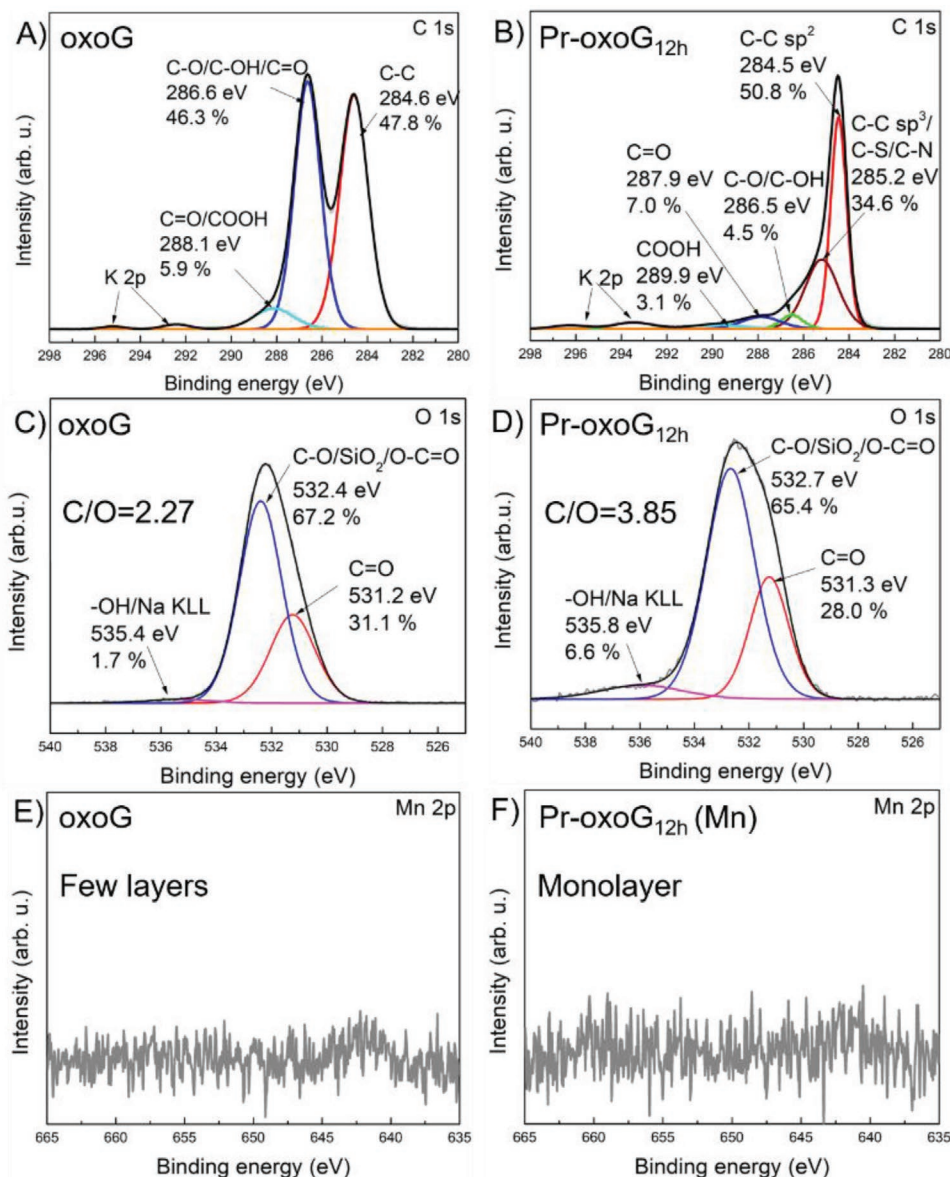
Figure 4. High-resolution C 1s (top) and O 1s (middle) spectra of (A), C) oxo-G, and B,D) Pr-oxoG$_{12h}$. High-resolution Mn 2p spectra (bottom) of E) oxo-G and F) Pr-oxoG$_{12h}$ (Mn).

Moreover, with growing pores into graphene the sp²-patches become smaller and consequently, the Raman spectra in Figure S9, Supporting Information, shows, as expected, a broadened D peak with $\Gamma_D = 106$ cm^{-1} for Pr-oxoG$_{12h}$, compared to $\Gamma_D = 84$ cm^{-1} for oxoG.

In the following, oxoG and Pr-oxoG$_{12h}$, respectively, are used to fabricate van-der-Waals heterostructures with a single-layer flake of MoS$_2$ deposited on top (illustrated in **Figure 5**). Raman spectra (Figure S10, Supporting Information) confirm that the transferred flake of MoS$_2$ is a monolayer by the measured difference between the out-of-plane A$_{1g}$ mode and the E$_{2g}$ mode of about 19.0 cm^{-1}, as typical for a monolayer.[46] For the fabrication of the heterostructures, we used a previously described procedure.[47] Figures 5B,D show optical microscopy images of the realized oxoG/MoS$_2$ and Pr-oxoG$_{12h}$/MoS$_2$ heterostructures,

respectively. The AFM images of the Pr-oxoG$_{12h}$/MoS$_2$ heterostructure is depicted in Figure S11A,B, Supporting Information, and proved the expected morphology.

The PL of MoS$_2$ on SiO$_2$, on oxoG, on Pr-oxoG$_{6h}$, and on Pr-oxoG$_{12h}$ are studied next. Figure 5E shows the respective PL of heterostructures. Obviously, the amplitude of the PL is increased for oxoG/MoS$_2$ and Pr-oxoG$_{12h}$/MoS$_2$, using pure MoS$_2$ on Si/SiO$_2$ substrate as internal reference, respectively, compared to the PL of the MoS$_2$ monolayer. The most intense PL is detected for Pr-oxoG$_{12h}$/MoS$_2$ with a 10-times increased amplitude. In contrast, the PL of Pr-oxoG$_{6h}$/MoS$_2$ is increased 3-times (Figure S12, Supporting Information) and for oxoG/MoS$_2$ a fourfold increased PL. As depicted in **Figure 6** there is a constant PL intensity over the complete flake, without any modulation. A related investigation demonstrated that
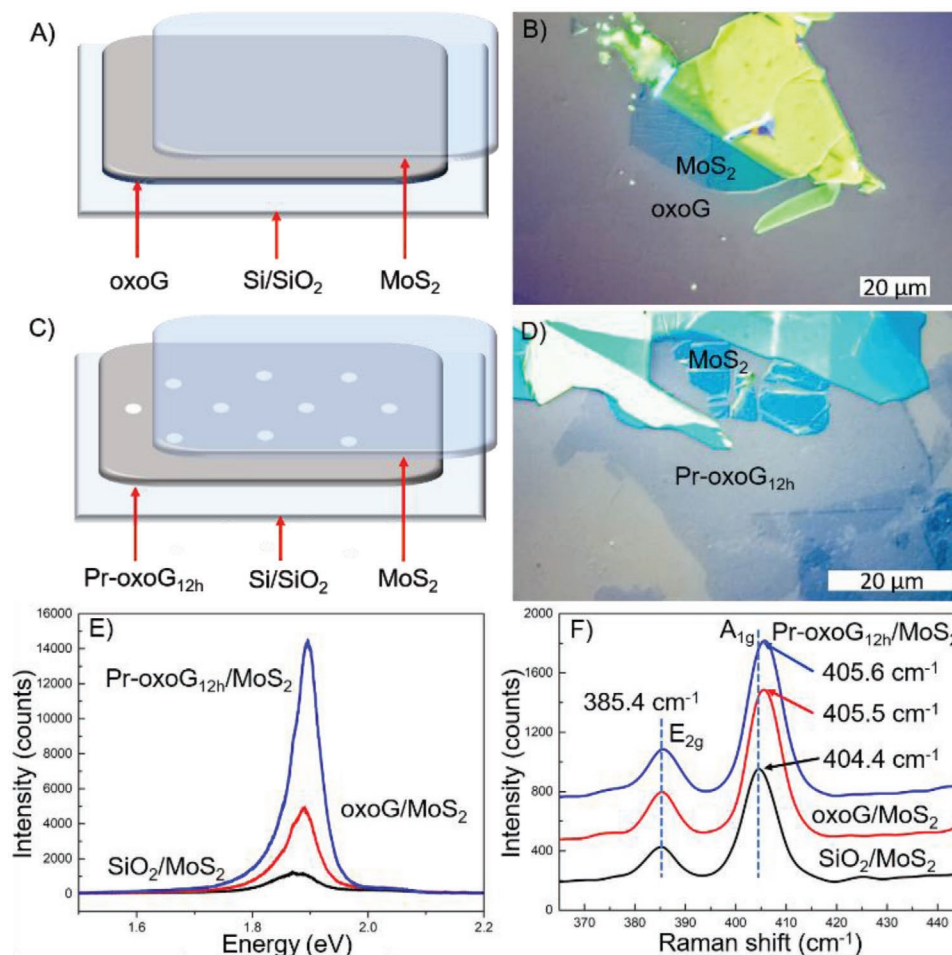
Figure 5. A) Illustration of the heterostructure of oxoG/MoS$_2$ and B) optical microscopy image of the realized oxoG/MoS$_2$ heterostructure. C) Illustration of the heterostructure of Pr-oxoG$_{12h}$/MoS$_2$ and D) optical microscopy image of the realized Pr-oxoG$_{12h}$/MoS$_2$ heterostructure. E) PL spectra of monolayer MoS$_2$ on SiO$_2$ (black), oxoG/MoS$_2$ (red), and Pr-oxoG$_{12h}$/MoS$_2$ (blue). F) Raman spectra of the same samples as in (E).

graphene oxide forms a p-type contact with monolayer MoS$_2$ and this is plausible due to electron-accepting groups detected by XPS, such as carbonyl groups.[48] Overall, the highest PL enhancement is achieved by using Pr-oxoG$_{12h}$. Figure 5F shows the Raman spectra of heterostructures detecting the A$_{1g}$ mode of MoS$_2$ in the heterostructures at around 404.4 cm^{-1}, which is blue-shifted to 405.5 and 405.6 cm^{-1} for MoS$_2$ on oxoG and Pr-oxoG$_{12h}$, respectively, while the position of E_{2g} mode is not shifted. Those observations indicate the p-doping of MoS$_2$ in the heterostructures by oxoG and Pr-oxoG$_{12h}$, respectively.[49,50] Moreover, Pr-oxoG$_{12h}$ reflects a p-doped graphene type material, as indicated by the analysis of the shifts of the G and 2D peak, respectively (Figure S15, Supporting Information). The p-doping effect of Pr-oxoG$_{12h}$ was further investigated by fabricating a heterostructure with a trilayer of MoS$_2$. Consistent with the expectations, the PL investigation (Figure S13, Supporting Information) indicates less enhancement (trilayer MoS$_2$ possesses an indirect band-gap), however, a fourfold increased PL is measured, compared to that of a monolayer MoS$_2$ with a direct band-gap on SiO$_2$. Thus, the highest, here 10-times increased PL is detected for assembled heterostructure of monolayer Pr-oxoG$_{12h}$/MoS$_2$.

In order to exclude the influence of remaining Mn-species on the PL, the PL enhancement of Pr-oxoG$_{12h}$ (Mn) (without HCl washing) was studied by forming the heterostructure of Pr-oxoG$_{12h}$ (Mn)/MoS$_2$. As shown in Figure S14, Supporting Information, the PL increases, however, only twice, indicating that full enhancement of PL is only achieved after HCl washing and the accompanied removal of particles. Thus, we speculate that Mn-species may form complexes with, for example, carbonyl groups at the rims of pores inhibiting the dramatic PL enhancement, although Raman spectra show the E_{2g} shift to 405.6 cm^{-1} for Pr-oxoG$_{12h}$ (Mn)/MoS$_2$. We note that the experimental observations give evidence for a p-doping effect by pore-graphene.

3. Conclusion

Here, we demonstrated the fabrication of graphene with circular pores on the 100 nm scale deposited on Si/SiO$_2$ surface by annealing of oxo-functionalized and potassium permanganate treated graphene flakes at 400 °C. While excess of Mn-species leads to heterogeneously formed pores and
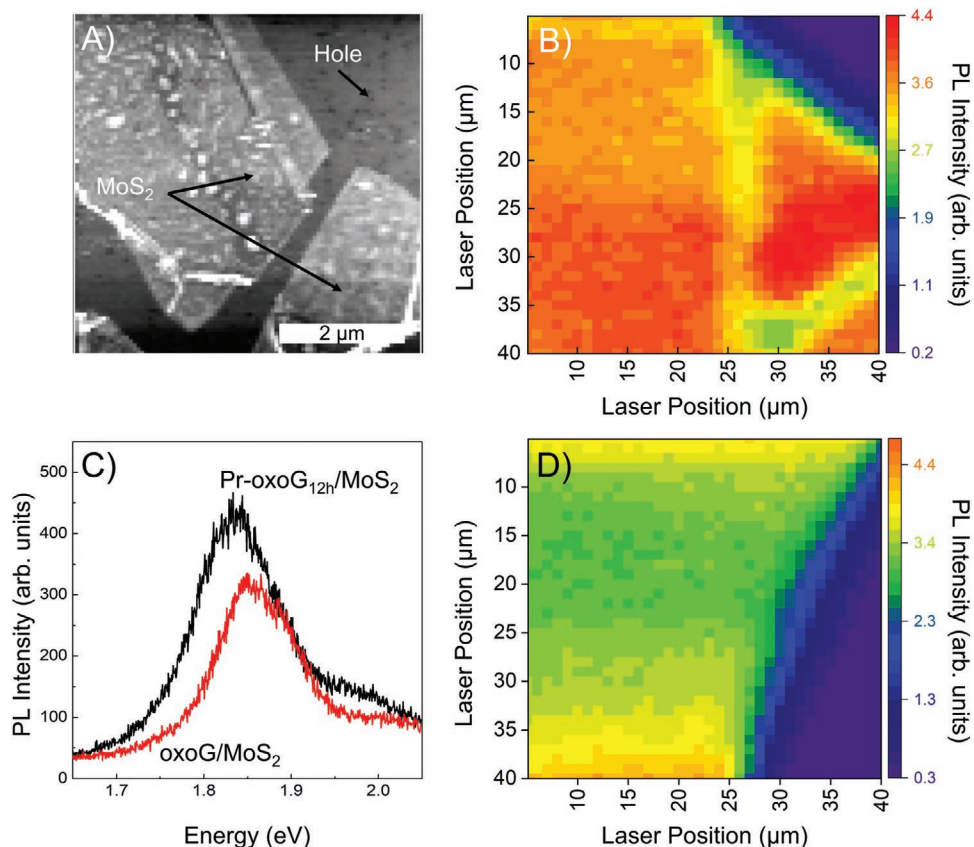
Figure 6. A) Features an AFM map of MoS_2 on top of Pr-oxoG$_{12h}$. Holes of sizes ranging from 50 nm to 200 nm are visible in the top right of the image and are well separated from one another. The Pr-oxoG$_{12h}$/MoS$_2$ PL intensity map (B) shows a constant PL intensity over the MoS_2 flake, exhibiting no sign of a spatial PL modulation that may arise from free-standing MoS_2. C) shows PL spectra from oxo-G/MoS$_2$ (red) and Pr-oxoG$_{12h}$/MoS$_2$ (black), the PL on the Pr-oxoG$_{12h}$ sample exhibiting higher intensity than that seen in the oxo-G/MoS$_2$ sample. A PL Intensity map of oxo-G/MoS$_2$ (D) taken with the same parameters as (B) shows a similar constant PL intensity in addition to having slightly lower intensity to that of Pr-oxoG$_{12h}$/MoS$_2$.

destroyed flakes, removal of excess potassium permanganate leads to the growth of circular pores with diameters of 50 to 250 nm, depending on the annealing time. Thereby, for example, uniform pores have mean diameters of 147 ± 73 nm after annealing for 12 h. From XPS analysis we conclude that carbonyl, hydroxyl, and carboxyl groups decorate the rims of pores. Since carbonyl groups have electron-accepting properties, it is plausible that the 2D material pore-graphene, can p-dope other 2D materials, such as MoS_2. However, further research, such as correlating field-effect measurements with PL mapping is necessary to further elucidate the mechanism behind PL enhancement by 10-times. Moreover, we showed that Mn-impurities limit the increase of the PL of MoS_2 in the heterostructure with pore-graphene and thus, we propose that the interaction of Mn-species with carbonyl groups may be responsible. Moreover, we conclude that not all defects detected by Raman spectroscopy lead to the growth of pores, taking into account that the initial distance of defects is 2 nm and the final pore-size increased to several hundreds of nm. Finally, we propose that pore-graphene is a 2D material with functional groups at the rims of pores and thus an attractive novel material for sensing applications in the future.

Supporting Information

Supporting Information is available from the Wiley Online Library or from the author.

Conflict of Interest

The authors declare no conflict of interest.

Data Availability Statement

The data that support the findings of this study are available from the corresponding author upon reasonable request.

[1] C. Neumann, D. Kaiser, M. J. Mohn, M. Füser, N.-E. Weber, O. Reimer, A. Gölzhäuser, T. Weimann, A. Terfort, U. Kaiser, A. Turchanin, *ACS Nano* **2019**, *13*, 7310.

[2] Z. Wang, Q. Yao, C. Neumann, F. Borrnert, J. Renner, U. Kaiser, A. Turchanin, H. J. W. Zandvliet, S. Eigler, *Angew. Chem., Int. Ed.* **2020**, *59*, 13657.

[3] F. Hao, D. Fang, Z. Xu, *Appl. Phys. Lett.* **2011**, *99*, 041901.

[4] B. Zhan, C. Li, J. Yang, G. Jenkins, W. Huang, X. Dong, *Small* **2014**, *10*, 399.

[5] D. Akinwande, C. J. Brennan, J. S. Bunch, P. Egberts, J. R. Felts, H. Gao, R. Huang, J.-S. Kim, T. Li, Y. Li, K. M. Liechti, N. Lu, H. S. Park, E. J. Reed, P. Wang, B. I. Yakobson, T. Zhang, Y.-W. Zhang, Y. Zhou, Y. Zhu, *Extreme Mech. Lett.* **2017**, *13*, 42.

[6] J. Xie, Q. Chen, H. Shen, G. Li, *J. Electrochem. Soc.* **2020**, *167*, 037541.

[7] K. G. Zhou, K. S. Vasu, C. T. Cherian, M. Neek-Amal, J. C. Zhang, H. Ghorbanfekr-Kalashami, K. Huang, O. P. Marshall, V. G. Kravets, J. Abraham, Y. Su, A. N. Grigorenko, A. Pratt, A. K. Geim, F. M. Peeters, K. S. Novoselov, R. R. Nair, *Nature* **2018**, *559*, 236.

[8] W. Wu, Y. Shi, G. Liu, X. Fan, Y. Yu, *Desalination* **2020**, *491*, 114452.

[9] H. Liu, H. Wang, X. Zhang, *Adv. Mater.* **2015**, *27*, 249.

[10] Q. Xu, H. Xu, J. Chen, Y. Lv, C. Dong, T. S. Sreeprasad, *Inorg. Chem. Front.* **2015**, *2*, 417.

[11] C. E. Halbig, R. Lasch, J. Krull, A. S. Pirzer, Z. Wang, J. N. Kirchhof, K. I. Bolotin, M. R. Heinrich, S. Eigler, *Angew. Chem., Int. Ed.* **2019**, *58*, 3599.

[12] A. Criado, M. Melchionna, S. Marchesan, M. Prato, *Angew. Chem., Int. Ed.* **2015**, *54*, 10734.

[13] S. Chen, J. Duan, M. Jaroniec, S. Z. Qiao, *J. Mater. Chem. A* **2013**, *1*, 9409.

[14] A. C. Lokhande, I. A. Qattan, C. D. Lokhande, S. P. Patole, *J. Mater. Chem. A* **2020**, *8*, 918.

[15] Y. Zhang, Q. Wan, N. Yang, *Small* **2019**, *15*, 1903780.

[16] A. Guirguis, J. W. Maina, L. Kong, L. C. Henderson, A. Rana, L. H. Li, M. Majumder, L. F. Dumée, *Carbon* **2019**, *155*, 660.

[17] X. Yang, C. Cheng, Y. Wang, L. Qiu, D. Li, *Science* **2013**, *341*, 534.

[18] S. Han, D. Wu, S. Li, F. Zhang, X. Feng, *Adv. Mater.* **2014**, *26*, 849.

[19] H. Yang, Q. He, Y. Liu, H. Li, H. Zhang, T. Zhai, *Chem. Soc. Rev.* **2020**, *49*, 2916.

[20] C. J. Russo, J. A. Golovchenko, *Proc. Natl. Acad. Sci. USA* **2012**, *109*, 5953.

[21] S. Standop, O. Lehtinen, C. Herbig, G. Lewes-Malandrakis, F. Craes, J. Kotakoski, T. Michely, A. V. Krasheninnikov, C. Busse, *Nano Lett.* **2013**, *13*, 1948.

[22] A. Guirguis, J. W. Maina, X. Zhang, L. C. Henderson, L. Kong, H. Shon, L. F. Dumée, *Mater. Horiz.* **2020**, *7*, 1218.

[23] N. I. Kato, *J. Electron Microsc.* **2004**, *53*, 451.

[24] Y. Lin, Y. Liao, Z. Chen, J. W. Connell, *Mater. Res. Lett.* **2017**, *5*, 209.

[25] S. P. Surwade, S. N. Smirnov, I. V. Vlassiouk, R. R. Unocic, G. M. Veith, S. Dai, S. M. Mahurin, *Nat. Nanotechnol.* **2015**, *10*, 459.

[26] T. He, Z. Wang, F. Zhong, H. Fang, P. Wang, W. Hu, *Adv. Mater. Technol.* **2019**, *4*, 1900064.

[27] A. Kaplan, Z. Yuan, J. D. Benck, A. Govind Rajan, X. S. Chu, Q. H. Wang, M. S. Strano, *Chem. Soc. Rev.* **2017**, *46*, 4530.

[28] X. Wang, L. Jiao, K. Sheng, C. Li, L. Dai, G. Shi, *Sci. Rep.* **2013**, *3*, 1996.

[29] H. Zhang, W. Liu, Z. Zhang, M. Li, B. Xu, J. Guo, *Phys. Chem. Chem. Phys.* **2018**, *20*, 26814.

[30] S. C. O'Hern, M. S. Boutilier, J. C. Idrobo, Y. Song, J. Kong, T. Laoui, M. Atieh, R. Karnik, *Nano Lett.* **2014**, *14*, 1234.

[31] L. Huang, M. Zhang, C. Li, G. Shi, *J. Phys. Chem. Lett.* **2015**, *6*, 2806.

[32] H.-K. Kim, S.-M. Bak, S. W. Lee, M.-S. Kim, B. Park, S. C. Lee, Y. J. Choi, S. C. Jun, J. T. Han, K.-W. Nam, K. Y. Chung, J. Wang, J. Zhou, X.-Q. Yang, K. C. Roh, K.-B. Kim, *Energy Environ. Sci.* **2016**, *9*, 1270.

[33] D. Zhou, Y. Cui, P. W. Xiao, M. Y. Jiang, B. H. Han, *Nat. Commun.* **2014**, *5*, 4716.

[34] Z. Fan, Q. Zhao, T. Li, J. Yan, Y. Ren, J. Feng, T. Wei, *Carbon* **2012**, *50*, 1699.

[35] Y. Xu, C.-Y. Chen, Z. Zhao, Z. Lin, C. Lee, X. Xu, C. Wang, Y. Huang, M. I. Shakir, X. Duan, *Nano Lett.* **2015**, *15*, 4605.

[36] S. Eigler, *Phys. Chem. Chem. Phys.* **2014**, *16*, 19832.

[37] S. Eigler, M. Enzelberger-Heim, S. Grimm, P. Hofmann, W. Kroener, A. Geworski, C. Dotzer, M. Rockert, J. Xiao, C. Papp, O. Lytken, H. P. Steinruck, P. Müller, A. Hirsch, *Adv. Mater.* **2013**, *25*, 3583.

[38] S. Eigler, F. Hof, M. Enzelberger-Heim, S. Grimm, P. Müller, A. Hirsch, *J. Phys. Chem. C* **2014**, *118*, 7698.

[39] M. M. Lucchese, F. Stavale, E. H. M. Ferreira, C. Vilani, M. V. O. Moutinho, R. B. Capaz, C. A. Achete, A. Jorio, *Carbon* **2010**, *48*, 1592.

[40] L. G. Cancado, A. Jorio, E. H. Ferreira, F. Stavale, C. A. Achete, R. B. Capaz, M. V. Moutinho, A. Lombardo, T. S. Kulmala, A. C. Ferrari, *Nano Lett.* **2011**, *11*, 3190.

[41] S. Eigler, C. Dotzer, F. Hof, W. Bauer, A. Hirsch, *Chem. - Eur. J.* **2013**, *19*, 9490.

[42] F. Grote, C. Gruber, F. Börrnert, U. Kaiser, S. Eigler, *Angew. Chem., Int. Ed.* **2017**, *56*, 9222.

[43] P. Feicht, J. Biskupek, T. E. Gorelik, J. Renner, C. E. Halbig, M. Maranska, F. Puchtler, U. Kaiser, S. Eigler, *Chem. - Eur. J.* **2019**, *25*, 8955.

[44] M. González, J. Baselga, J. Pozuelo, *J. Mater. Chem. C* **2016**, *4*, 8575.

[45] K. Garg, R. Shanmugam, P. C. Ramamurthy, *Opt. Mater.* **2018**, *76*, 42.

[46] C. Lee, H. Yan, L. E. Brus, T. F. Heinz, J. Hone, S. Ryu, *ACS Nano* **2010**, *4*, 2695.

[47] Z. Wang, Q. Yao, Q. Hu, C. Li, M. Hußmann, B. Weintrub, J. N. Kirchhof, K. Bolotin, T. Taniguchi, K. Watanabe, S. Eigler, *RSC Adv.* **2019**, *9*, 38011.

[48] T. Musso, P. V. Kumar, A. S. Foster, J. C. Grossman, *ACS Nano* **2014**, *8*, 11432.

[49] X. Wei, Z. Yu, F. Hu, Y. Cheng, L. Yu, X. Wang, M. Xiao, J. Wang, X. Wang, Y. Shi, *AIP Adv.* **2014**, *4*, 123004.

[50] W. Zhang, J.-K. Huang, C.-H. Chen, Y.-H. Chang, Y.-J. Cheng, L.-J. Li, *Adv. Mater.* **2013**, *25*, 3456.